Article

Reversible Electrochemical Lithium Cycling in a Vanadium(IV)- and Niobium(V)-Based Wadsley−Roth Phase

Erick A. Lawrence, Matthew A. Davenport, Reshma Devi, Zijian Cai, Maxim Avdeev, Jonathan R. Belnap, Jue Liu, Husain Alnaser, Alice Ho, Taylor D. Sparks, Gopalakrishnan Sai Gautam, Jared M. Allred,* and Huiwen Ji*

Cite This: https://doi.org/10.1021/acs.chemmater.2c03465

Read Online

ACCESS | Metrics & More | Article Recommendations | Supporting Information

ABSTRACT: Fast charging remains one of the greatest safety challenges in Li-ion batteries due to Li-dendrite growth occurring on graphite anodes if they are lithiated too quickly. The search for high-rate anodes has highlighted materials in the Wadsley−Roth (WR) shear phase family. The relative abundance of V compared with traditional WR compositions of Nb and W makes V-based phases attractive. However, the high voltage and poor reversibility typically associated with V redox have made V-rich WR phases less studied than Nb- and W-rich phases. Here, we show that a new V-rich Wadsley−Roth phase, $V_7Nb_6O_{29}$, achieves excellent rate capability and 80% capacity retention after 228 cycles with a relatively low average voltage of 1.76 V vs Li/Li$^+$ compared with other V-rich WR phases. Single-crystal X-ray diffraction reveals a $P4/m$ space group with repeating $2 \times 2 \times \infty$ and $3 \times 3 \times \infty$ blocks of V^{4+} and Nb^{5+} octahedra. Combined neutron pair distribution function analysis, X-ray absorption spectroscopy, and density functional theory calculations show that V redox is the primary source of capacity and that cycling stability is provided by the stable octahedral coordination adopted by V^{4+} in the material.
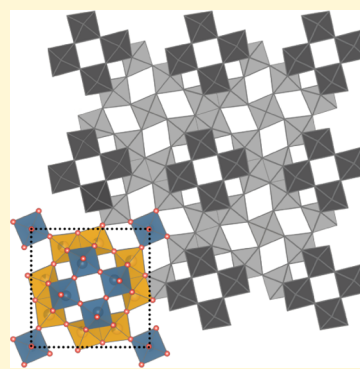
INTRODUCTION

As the automotive industry increasingly transitions to electric vehicles, the demand for Li-ion battery technology has caused unprecedented growth in the energy storage industry. Market research has estimated that the global market size of lithium-ion batteries will exceed $180 billion by 2030.[1] Further advancements in Li-ion battery technology must be made before the widespread electrification of personal transportation can occur, chiefly requiring a decrease in charging time and an increase in power performance. Both metrics are fundamentally limited in state-of-the-art Li-ion batteries because of the poor rate capability of the graphite anodes commonly used. When graphite is lithiated faster during charging than its effective Li-ion uptake rate, metallic lithium plating, electrolyte degradation, and severe dendrite growth can occur, which causes short circuits and thermal runaway, posing a significant safety hazard.[2−5]

To address the persistent safety and fast charging challenges associated with conventional graphite anodes, extensive research has focused on identifying promising alternatives such as $Li_4Ti_5O_{12}$,[6−9] modified graphite,[10−12] Nb_2O_5,[13−16] TiO_2,[17−19] ReO$_3$-type phases,[20−25] and a recently developed disordered-rocksalt-type phase.[26] Among them, the prototypical ReO$_3$ structure features a three-dimensional (3D) corner-sharing ReO$_6$ octahedral network that hosts open channels for Li intercalation. Derivatives of the ReO$_3$ structure can be obtained by replacing the hexavalent element with lower-valent species such as Nb^{5+}, Ti^{4+}, and V^{5+}, which introduces oxygen vacancies that are structurally compensated for through octahedral edge sharing or forming filled pentagonal channels. Such octahedral networks can stabilize the lattice during lithiation against unfavorable tilt distortions that typically impede Li diffusion in classic ReO$_3$ structures.[20,23−25] These early-transition-metal (TM) ReO$_3$ derivatives have seen a recent resurgence in interest for use as Li-ion anodes since the landmark studies by Griffith and colleagues,[20,22] which demonstrated ultrahigh rate capability, as well as long-term cycling stability (at 20C using micron-sized particles) in Nb(V)- and W(VI)-based WR and tetragonal tungsten bronze (TTB) anodes.[20] In addition, their operating voltages between 1 and 2 V vs Li$^+$/Li can avoid detrimental solid−electrolyte interphase formation and electrolyte degradation.

Many more early-TM oxides containing Ti, Nb, Mo,[27] and W have been identified as potential Li-ion anodes. The vast majority of them are Nb-based, such as $TiNb_2O_7$ (WR),[28] NbO_2F (ReO$_3$-type),[29,30] Nb_3O_7F (WR),[29] $Nb_{16}W_5O_{55}$

(WR),[20,22] $Nb_{18}W_{16}O_{93}$ (TTB),[20] $Nb_{18}W_8O_{69}$ (TTB),[21] Nb_2O_5 polymorphs,[31] and PNb_9O_{25} (WR).[32] In comparison, only a handful of V-containing phases have been explored as Li-ion anodes although V is more earth-abundant than Nb.[33] An early example was demonstrated in V_6O_{13} as a proof of concept, where the material had a relatively high average discharge voltage of ~2.3 V, much higher than most other early-TM oxide anodes, from the involvement of V^{4+}-to-V^{5+} redox and yielded ~0.9 Li per TM capacity.[34] The V_6O_{13} study noted that the sheared structure stabilizes performance relative to similar nonsheared compositions.[34] Another V-based WR phase with mixed TMs, $(W_{0.2}V_{0.8})_3O_7$, crystallizes in a $3 \times 3 \times \infty$ structure with mixed V^{4+}, V^{5+}, and W^{6+} and exhibits high rate capability and cycling stability.[35] Its average discharge voltage is around 2.2 V, likely due to the involvement of V^{4+}-to-V^{5+} redox. A third V-based material, VNb_9O_{25}, contains minimal V but shows significantly more irreversible capacity loss and smaller capacity than its analogue PNb_9O_{25}, which is partially attributed to irreversible V^{5+}-to-V^{3+} reduction and the associated migration of V^{5+} upon delithiation.[36] Therefore, it is of great interest to develop a ReO_3-derivative anode that utilizes V redox of a 4+ valence and below to lower the operating voltage for a maximized cell energy density and avoid any irreversible V migration due to the different coordination environment of V^{5+} from its reduced counterparts.

In this paper, we present the synthesis, structural, and electrochemical characterizations of $V_7Nb_6O_{29}$, a new member of the Wadsley–Roth family. First discovered as a byproduct during vapor transport growth, its structure was unambiguously solved by single-crystal diffraction refinement and is identified to host both $3 \times 3 \times \infty$ and $2 \times 2 \times \infty$ blocks of TM octahedra that extend one-dimensionally. The notations "$3 \times 3 \times \infty$" and "$2 \times 2 \times \infty$" represent the numbers of octahedra along the a, b, and c axes within the characteristic blocks. The compound can be viewed as the sum of three Nb_2O_5 and seven VO_2 based on its formula units. Lithiation is expected to reduce the transition-metal (TM) species to V^{3+} and Nb^{4+}, and at most, V^{2+} and Nb^{3+}, which all favor octahedral coordination and minimal irreversible TM migration during Li (de)intercalation for stable cycling. It delivers a discharge capacity of 208 mAh/g (roughly 11.0 Li/formula unit) when cycled between 1.2 and 3.3 V vs Li/Li+. While the average voltage of $V_7Nb_6O_{29}$ (1.76 V vs Li/Li+) is higher than many V-free ReO_3-derivative anodes (~1.5 V vs Li/Li+),[22,32] it compares favorably to other V-rich ReO_3-derivative phases and represents a step forward for lower-voltage V-rich WR phases. We demonstrate good rate capability, stable cycling, and probe the TM ordering using neutron diffraction and pair distribution function (PDF) analysis. X-ray absorption near-edge spectroscopy (XANES) and density functional theory (DFT) calculations reveal Nb contributes marginally to the redox behavior, with most activity occurring on V, from a mixed V^{2+}/V^{3+} to V^{4+}.

EXPERIMENTAL SECTION

Single-Crystal Growth. Single-crystal synthesis was performed by mixing stoichiometric amounts of VO_2 (Materion, 99.5%) and NbO_2 (Aldrich, 99.9%) with the target composition of $V_{0.10}Nb_{0.90}O_2$. Between 0.3 and 0.6 g reagents were sealed in an evacuated fused quartz ampoule (1 cm diameter, ~23 cm long) with 0.15 mg $TeCl_4$ (Alfa Aesar, 99.9%) as a transport agent. Growth was performed in a single-zone furnace set to 950 °C ramped at 1.5 °C/min with the end left open to air resulting in a natural temperature gradient of 950 °C in the hot zone and roughly 850 °C in the cold zone. The resulting

products contained a mixture of vanadium and niobium oxides with an additional unknown material. A crystal of this unknown composition was isolated and used for single-crystal X-ray diffraction (SXRD) experiments and crystal structure determination. The determined structure yielded the formula $V_7Nb_6O_{29}$, which was then used to inform the powder synthesis methods.

Powder Synthesis. Polycrystalline $V_7Nb_6O_{29}$ was synthesized via a conventional solid-state method. All precursors were handled in an Ar-filled glovebox (MBraun). Synthesis used V_2O_5 (Sigma-Aldrich, 98%), Nb metal (Sigma-Aldrich, 99.8%), and Nb_2O_5 (Sigma-Aldrich, 99.9%) as precursors. V_2O_5 was used in 5% excess to compensate for loss during handling because the powder easily stuck to the surface of mixing media and containers. Furthermore, fresh V_2O_5 was transferred into the glovebox for each synthesis to avoid decomposition in the oxygen-bare environment. Stoichiometric amounts of all precursors were gently ground in an agate mortar and pestle for 5 min before being placed in a hardened-steel shaker mill jar (SPEX) along with sixteen 5 mm steel balls (SPEX), sealed, and shaken in a SPEX 8000M mixer mill for 15 min. The precursors were then collected from the container by scraping the sides of the walls with a stainless steel spatula and pressed into 6 mm pellets under 1 ton of force. The precursor pellets were wrapped together in gold foil and vacuum sealed in quartz ampoules. The ampoules were heated at 1 °C/min to 650 °C and held for 10 h, then the temperature was increased at 1 °C/min to 850 °C and held for 16 h. Finally, the ampoules were cooled at 3 °C/min to room temperature. The ampoules were then transferred into an Ar glovebox to collect the pellets from the ampoules and gently grind the pellets to a powder using an agate mortar and pestle.

Structural Characterization. Single-crystal diffraction data were collected using a Rigaku Synergy-R DW operating in the Mo Kα mode and equipped with a Hypix 6000HE detector. Data reduction and absorption correction were handled in the CrysAlisPro software suite. Structural models of the single-crystal diffraction data were solved and refined using SHELX[37] and WINGX.[38] Crystal structures are visualized using VESTA.[39]

High-resolution neutron powder diffraction (NPD) experiment was carried out at room temperature on the diffractometer ECHIDNA at the OPAL research reactor operated by the Australian Nuclear Science and Technology Organisation (ANSTO).[40] Approx. 0.7 g of powder sample was loaded in an Ar-filled glovebox to a cylindrical vanadium can of 6 mm diameter and NPD data were collected using a constant wavelength of 1.6220(5) Å. Rietveld analysis of the NPD data was performed using the GSAS code[41] with EXPGUI front end.[42]

Neutron diffraction and pair distribution function (NPDF) measurement was also performed at the time-of-flight neutron Beamline 1B NOMAD at the Spallation Neutron Source (SNS) of Oakridge National Laboratory. The sample was packed into a quartz glass capillary of 3 mm diameter in an Ar-filled glovebox. Powder packing density was estimated to be 50−60% (loose random packing). Data refinement was performed using the PDFGUI[43] software package for NPDF and TOPAS for diffraction. The resolutions for Echidna and NOMAD are ~0.1 and 0.24%, respectively.

A STOE STADI-P powder X-ray diffractometer equipped with Mo anode Kα₁ radiation, a Ge(111) curved monochromator, and a Dectris MYTHEN2 detector was used in transmission geometry. Ex situ diffraction patterns were collected at room temperature in moving mode across the 2θ range of 2−40° from $V_7Nb_6O_{29}$ electrode films pre-cycled to designated states of charge. The lattice dimension change was deduced from Le Bail fitting using the GSAS-II[44] software package.

To determine the particle size of the active material, scanning electron microscopy (SEM) was carried out at the University of Utah Nanofab Surface Analysis Lab using an FEI Quanta 600F scanning electron microscope at 20 kV.

Lithiated powder samples for neutron diffraction were prepared by pressing ~40 mg pellets of as-synthesized $V_7Nb_6O_{29}$ powder. Half-cells (CR2032) were assembled using stainless steel cathode caps,
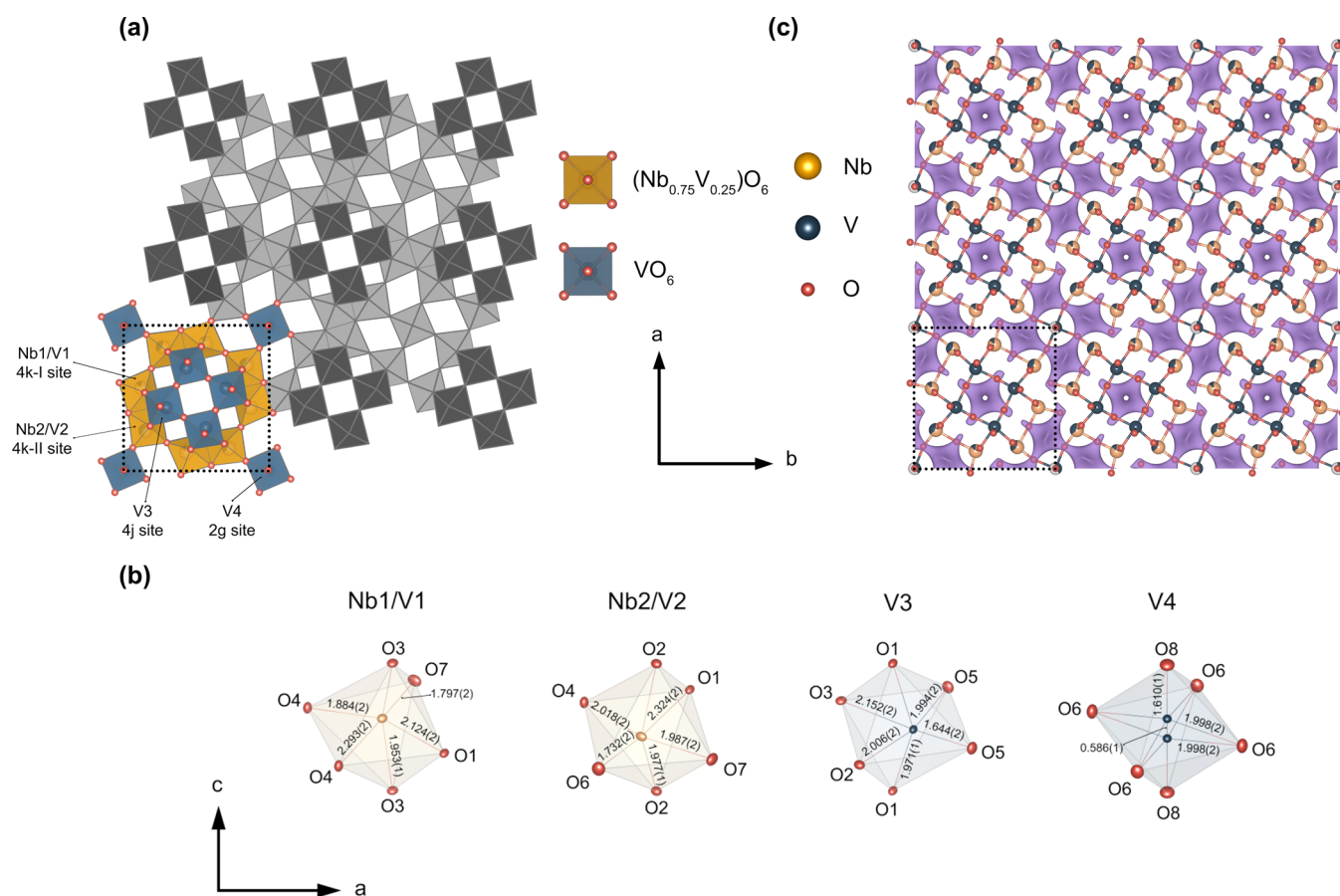
Figure 1. (a) Crystal structure of $V_7Nb_6O_{29}$. A tetragonal unit cell viewed down c is outlined in the lower left corner. The structure is composed of $3 \times 3 \times \infty$ blocks of corner-sharing NbO_6 and VO_6 octahedra as well as $2 \times 2 \times \infty$ blocks of corner-sharing VO_6 octahedra. Blocks are connected through octahedral edge sharing. The $2 \times 2 \times \infty$ and $3 \times 3 \times \infty$ blocks are depicted as dark gray and light gray clusters, respectively, in the extended schematic. (b) Local coordination environment of each crystallographically unique cation site. Atomic displacements are displayed as anisotropic ellipsoids. Unmarked bond lengths are equivalent to the opposite marked bond. (c) Purple isosurface of Li potential calculated using a BVSE method and overlaid on the crystal structure. Li-conduction pathways are organized into $2 \times 2 \times \infty$ and $1 \times 1 \times \infty$ channels.

anode caps, springs, glass microfiber filters (Whatman), 1 M $LiPF_6$ in ethylene carbonate and dimethyl carbonate (EC/DMC) solution (1:1, Sigma-Aldrich), and Li-foil (Sigma) that had been polished on both sides with a soft plastic spatula to ensure good electrical and electrochemical contact. Cells were assembled in an argon glovebox (MBraun) using a coin cell crimper (Wellcos) and rested for 6 h to ensure proper electrolyte wetting before being discharged galvanostatically at 5 mA/g to 1.2 V vs Li/Li$^+$ followed by constant voltage trickle charging with a cutoff current 0.5 mA/g to ensure complete powder lithiation (Arbin battery cycler, 25 °C). Cells were then disassembled and the lithiated $V_7Nb_6O_{29}$ pellets were recovered, crushed, then washed twice with DMC (99+% extra dry, Acros Organics) to remove electrolyte salts. The electrochemically lithiated sample was measured by neutron diffraction at the time-of-flight neutron Beamline 1B NOMAD at the Spallation Neutron Source (SNS) of Oakridge National Laboratory under the same conditions as the pristine sample for NPDF. The resultant diffraction pattern was refined by constraining the Li amount of 13 Li/f.u. as observed from the electrochemical capacity (~253 mAh/g) under the slow discharging and equilibration conditions.

Electrochemistry. Free-standing electrode films were fabricated from the polycrystalline $V_7Nb_6O_{29}$ active material, carbon black (Alfa Aesar, 99%), and PTFE (Sigma-Aldrich) with a weight ratio of 8:1:1. To ensure intimate mixing, 240 mg as-synthesized $V_7Nb_6O_{29}$ and 30 mg carbon black were shaker-milled for 10 min and recovered. An agate mortar and pestle were used to grind 90 mg of the shaker-milled mixture with 10 mg PTFE until all powder had been incorporated into a shaggy mass. A clean stainless steel work surface and rolling pin

were used to roll the electrode mass flat which was then folded and rolled parallel to the fold. This was performed six more times (for a total of seven folds) before the electrode mass was rolled into a thin film. Electrodes were cut from the film using an 8 mm stainless steel punch and were rolled and trimmed until the original approximate area was conserved and electrodes achieved a mass between 1 and 1.5 mg. Half-cells were then assembled (using the same process as described above for lithiated powder samples) and rested for 6 h to ensure proper electrolyte wetting before being cycled galvanostatically at 25 °C on an Arbin battery cycler. Cyclic voltammetry was performed using a BioLogic SP-300 potentiostat.

X-ray Absorption Near-Edge Spectroscopy (XANES). Ex situ XANES measurements were conducted in transmission mode at room temperature using beamline 20-BM at the Advanced Photon Source at Argonne National Laboratory. The prepared XANES samples (electrode films cycled to designated states of charge) were sealed with polyimide tape (Kapton, DuPont) on both sides to prevent air exposure. The incident energy was selected using a Si(111) monochromator and a Rh-coated mirror was used to minimize high-order harmonics. The energy calibration was performed by simultaneously measuring the spectra of V or Nb metal foils. The obtained XANES data were analyzed using the Athena[45] software package.

SoftBV. Empirical bond valence site energy (BVSE) calculation was performed using the SoftBV software tool.[46] Constant BVSE isosurfaces were plotted using VESTA[39] to visualize potential Li migration pathways.

Density Functional Theory (DFT) Calculations. The unit cells of $V_7Nb_6O_{29}$ and $Li_{13}V_7Nb_6O_{29}$ were fully relaxed (cell shape, size, and ionic positions), and the corresponding total energies and atomic forces were calculated using density functional theory (DFT),[36,37] as implemented in the Vienna Ab initio Simulation Package (VASP),[38,39] which employs the projector-augmented wave (PAW[40]) potentials to treat the core electrons. A plane-wave-basis kinetic energy cutoff of 520 eV and a fully automatic Γ-centered k-point grid generation scheme with a density of 48 eV/Å were used to sample the irreducible Brillouin zone. The structures were relaxed until the total energy and forces were below a threshold of 10^{-5} eV and |0.01| eV/Å, respectively, with the relaxations performed without any symmetry constraints. The electronic exchange–correlation (XC) interactions during the structure relaxations were treated by the strongly constrained and appropriately normed (SCAN[41]) functional with an effective on-site Hubbard U[44] correction applied on V ions only (U_V = 1 eV[43]). The Heyd–Scuseria–Ernzerhof (HSE06[42]) hybrid exchange–correlation functional was used for the DOS calculations to obtain a better description of the on-site magnetic moments of the V and Nb ions in the lithiated and delithiated phases of $V_7Nb_6O_{29}$. The "fake" self-consistent field (SCF) method was used to obtain the electronic density of states (DOS), wherein the converged geometry from the SCAN structure relaxation was taken as the input with a mesh density of 16 k-points per Å.

■ RESULTS

Synthesis and Electrochemistry. Based on the refinement of single-crystal X-ray diffraction, $V_7Nb_6O_{29}$ adopts the $P4/m$ (No. 84) space group. The structure has sheared blocks characteristic of WR phases when viewed down the c-axis. Sheared blocks manifest in two types, namely, $2 \times 2 \times \infty$ blocks with only corner-sharing VO_6 octahedra and $3 \times 3 \times \infty$ blocks with a VO_6 center surrounded by 8 octahedra of mixed V/Nb occupancy in the same ab plane (Figure 1a). Accordingly, the sheared planes along the boundaries between blocks are all parallel to the c-axis. The experimental, data reduction, and structural refinement parameters from the SXRD experiment are presented in Table 1. The resulting atomic parameters of the structural model are presented in Tables 2 and 3.

The single-crystal structure solution tested mixed occupancy on each metal site separately by allowing a refined total occupancy of Nb and V that summed to 1. Two sites (Nb1/V1 and Nb2/V2, 4k Wyckoff site) showed clear improvement with a mixed occupancy of 86.0(4) % and 64.0(3) % Nb, respectively. The mixed sites were treated as a single position in terms of the fractional coordinates and thermal parameters of the Nb and V components. To differentiate the Nb1/V1 and Nb2/V2 sites which both occupy 4k Wyckoff positions, hereafter, the Nb1/V1 sites are denoted as 4k-I sites while the Nb2/V2 sites are denoted as 4k-II sites. Allowing mixed occupancy on the third metal site (V3, 4j Wyckoff site) leads to a negative Nb occupancy and an unstable model, and so this site was treated as purely V. The fourth metal site (V4, 2g Wyckoff site) is displaced from its octahedral center by about 0.3 Å in an apparently disordered manner, with the site being split across two possible locations. The site can be treated as fully occupied by V with a good agreement between the model and observation. The addition of Nb on this site in the same manner as Nb1 and Nb2 yields a refined Nb occupancy of about 5.4(6)%. From a purely statistical perspective (using the Hamilton R-test), the addition of Nb is a significant improvement to a pure V site on this crystallographic site.

To balance this observation, it must also be noted that the crystallographic model does not account for the effects of local

Table 1. Crystal Structure Refinement Data and Parameters from the Single-Crystal X-ray Diffraction Experiment

space group type	$P4/m$
crystal system	tetragonal
formula (refined)	$V_{7.00(4)}Nb_{6.00(4)}O_{29}$
a (Å)	11.82077(17)
c (Å)	3.80816(9)
V (Å^3)	531.81(2)
Z	1
temperature	299.91(10) K
crystal size (μm)	167, 59, 34
λ	0.71073
μ (mm^{-1})	6.153
scan mode	ω-scans
absorption correction	Gaussian
T_{min}, T_{max}	0.419, 0.873
reflections measured, unique, used	8523, 1567, 1525
resolution (d_{min}, $2\theta_{max}$)	0.576 Å, 76.158°
$(hkl)_{max}$	(20 20 6)
R_{int}	1.41%
R_σ	0.95%
parameters	68
method of refinement	shelx, $|F^2|$
wR_2 (all, obs)	3.77%, 3.74%
R_1 (all, obs)	1.56%, 1.48%
GOF	1.321
F_{000}	639
max residual density	0.48, −0.92
CSD code	2239390

structural correlations on the diffracted peak intensity. It is reasonable to expect some kind of short-range correlations from the positional disorder on this metal site that cannot be modeled in this crystallographic model. Treating the V4 site as purely V yields the stoichiometry $V_{7.00(4)}Nb_{6.00(4)}O_{29}$. The local coordination of each cation site is depicted in Figure 1b.

The resulting polycrystalline product from solid-state synthesis at 850 °C has a graphite black color, which suggests partial d orbital occupation in the TM species and the possibility of good electrical conductivity. The calcination temperature was carefully selected after extensive optimization to avoid incomplete reaction or decomposition. Note that a parallel synthesis attempt starting from a Nb_2O_5 and VO_2 mixture at 850 °C generated minimal reaction between the precursors and we suspect the involvement of low-melting V_2O_5 (690 °C mp) is critical for facilitating the reaction and obtaining the target phase.

Probable Li transport pathways are estimated by empirical BVSE calculations. A testing Li-ion is sequentially placed at points on a three-dimensional grid over an entire unit cell to search for pathways of low bond valence mismatch, which are energetically favorable channels for Li diffusion. The iso-surfaces of Li-ion site energy are taken to be 1.0 eV over the global minimum and are plotted in purple (Figure 1c). The iso-surfaces are connected $2 \times 2 \times \infty$ and $1 \times 1 \times \infty$ dodecahedra within the $3 \times 3 \times \infty$ and $2 \times 2 \times \infty$ blocks, respectively, and forming channels down the c-axis. The observation suggests the viable candidacy of this material for use as a Li-ion intercalation electrode and is consistent with other WR anodes in which Li diffusion mostly occurs within such block channels.[21,22]

Table 2. Atomic Sites and Positions from the Single-Crystal X-ray Diffraction Experiment and Structural Refinement

atom	site	x	y	z	U_{iso} (Å^2)	occupancy
O1	4k	0.74896(9)	0.55900(9)	1/2	0.00608(16)	1
O2	4j	0.81833(9)	0.69539(9)	0	0.00655(16)	1
O3	4j	0.85623(9)	0.46369(9)	0	0.00663(16)	1
O4	4k	0.03220(9)	0.39491(9)	1/2	0.00732(17)	1
O5	4j	0.58517(9)	0.63506(9)	0	0.00888(18)	1
O6	4k	0.93788(10)	0.84474(10)	1/2	0.01122(19)	1
O7	4k	0.81052(10)	0.29702(9)	1/2	0.01010(19)	1
O8	1a	0	0	0	0.0118(4)	1
Nb1	4k	0.87755(2)	0.43336(2)	1/2	0.00575(4)	0.860(4)
Nb2	4k	0.84949(2)	0.72805(2)	1/2	0.00630(5)	0.640(3)
V1	4k	0.87755(2)	0.43336(2)	1/2	0.00575(4)	0.140(4)
V2	4k	0.84949(2)	0.72805(2)	1/2	0.00630(5)	0.360(3)
V3	4j	0.70666(2)	0.56749(2)	0	0.00493(6)	1
V4	2g	0	0	0.42279(17)	0.00506(11)	1/2

atom	site	x	y	z	U_{iso} (Å^2)	occupancy
O1	4k	0.74896(9)	0.55900(9)	1/2	0.00608(16)	1
O2	4j	0.81833(9)	0.69539(9)	0	0.00655(16)	1
O3	4j	0.85623(9)	0.46369(9)	0	0.00663(16)	1
O4	4k	0.03220(9)	0.39491(9)	1/2	0.00732(17)	1
O5	4j	0.58517(9)	0.63506(9)	0	0.00888(18)	1
O6	4k	0.93788(10)	0.84474(10)	1/2	0.01122(19)	1
O7	4k	0.81052(10)	0.29702(9)	1/2	0.01010(19)	1
O8	1a	0	0	0	0.0118(4)	1
Nb1	4k	0.87755(2)	0.43336(2)	1/2	0.00575(4)	0.860(4)
V1	4k	0.87755(2)	0.43336(2)	1/2	0.00575(4)	0.140(4)
Nb2	4k	0.84949(2)	0.72805(2)	1/2	0.00630(5)	0.640(3)
V2	4k	0.84949(2)	0.72805(2)	1/2	0.00630(5)	0.360(3)
V3	4j	0.70666(2)	0.56749(2)	0	0.00493(6)	1
V4	2g	0	0	0.42279(17)	0.00506(11)	1/2

Table 3. Anisotropic Thermal Parameters from the Single-Crystal X-ray Diffraction Structure Solution and Refinement

atom	U_{11}	U_{22}	U_{33}	U_{12}
O1	0.0062(4)	0.0081(4)	0.0040(4)	0.0016(3)
O2	0.0078(4)	0.0070(4)	0.0048(4)	−0.0009(3)
O3	0.0086(4)	0.0075(4)	0.0037(4)	0.0009(3)
O4	0.0056(4)	0.0073(4)	0.0090(4)	0.0009(3)
O5	0.0068(4)	0.0086(4)	0.0112(5)	0.0023(3)
O6	0.0117(4)	0.0077(4)	0.0143(5)	−0.0010(3)
O7	0.0119(4)	0.0086(4)	0.0098(4)	−0.0041(3)
O8	0.0144(6)	U_{11}	0.0065(8)	0
Nb1	0.00675(6)	0.00571(6)	0.00479(6)	0.00087(3)
V1	0.00675(6)	0.00571(6)	0.00479(6)	0.00087(3)
Nb2	0.00784(7)	0.00561(6)	0.00546(7)	−0.00229(4)
V2	0.00784(7)	0.00561(6)	0.00546(7)	−0.00229(4)
V3	0.00472(9)	0.00597(10)	0.00411(10)	0.00103(6)
V4	0.00549(13)	U_{11}	0.0042(2)	0

Taking advantage of the excellent contrast between the neutron scattering lengths of V and Nb (−0.38 and 7.05 fm, respectively, i.e., the scattering length of V is almost negligible compared to Nb), neutron diffraction was performed to verify the purity of the as-prepared $V_7Nb_6O_{29}$ polycrystalline phase. The Rietveld refinement is shown in Figure 2a, and the associated fit parameters are listed in Table S1. The rising background at low angles is due to air scattering from the area close to the sample while the uniform background scattering is contributed by incoherent V scattering arising from both the V contained in the sample (∼0.18 g) as well as the V sample

holder (∼0.7 g). Since the mass of the V in the sample was low compared with the mass of the V sample holder, the V in the sample likely did not contribute to increased background scattering compared with other V-free samples. As is common in WR and other ReO_3-derivative anodes, there is some degree of TM disorder. Given that the metal sites are fully occupied based on single-crystal diffraction, the V and Nb fractions could be constrained to occ(Nb) + occ(V) = 1. The small scattering length of V provided strong neutron scattering contrast between V and Nb and allowed the accurate determination of their distribution. Mixed Nb and V occupancy is found in two 4k Wyckoff positions, which are the eight octahedral sites surrounding a central VO_6 in the 3 × 3 block plane. The 4k-I site was refined to 87.1(8)% Nb occupancy and 12.9(8)% V occupancy, and the 4k-II site was refined to 63.0(7)% Nb occupancy and 37.0(7)% V occupancy. The refined occupancies are very close to the values obtained from single-crystal data. The resulting site occupancies correspond to the total composition of 6.00(6) Nb per formula unit and 2.00(6) V per formula unit. Since there are 5 more pure V sites distributed throughout the structure, the overall chemical formula can be determined as $V_{7.00}Nb_{6.00}O_{29}$ which is within the error of refinement of the idealized formula of $V_7Nb_6O_{29}$. Given the large number of inequivalent O sites and high peak overlap, the refinement of their thermal displacements was constrained to be isotropic. Note that the thermal displacements obtained from ECHIDNA are systematically smaller than those from single-crystal refinement due to the absence of absorption correction in ECHIDNA-NPD refinement.
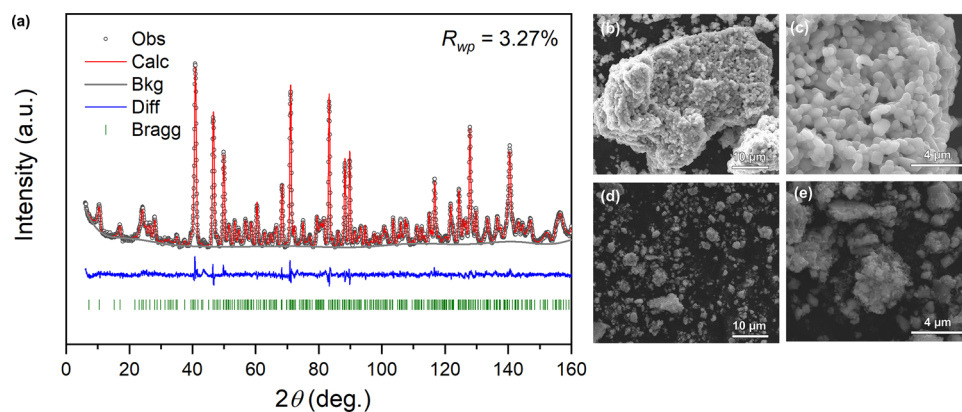
Figure 2. (a) Refinement of powder neutron diffraction data on single-phase $V_7Nb_6O_{29}$ collected on ECHIDNA at room temperature. SEM images of (b, c) the as-prepared $V_7Nb_6O_{29}$ powders with submicron crystallites agglomerated in large (>15 μm) secondary particles and (d, e) the powders after being shaker-milled with carbon black.
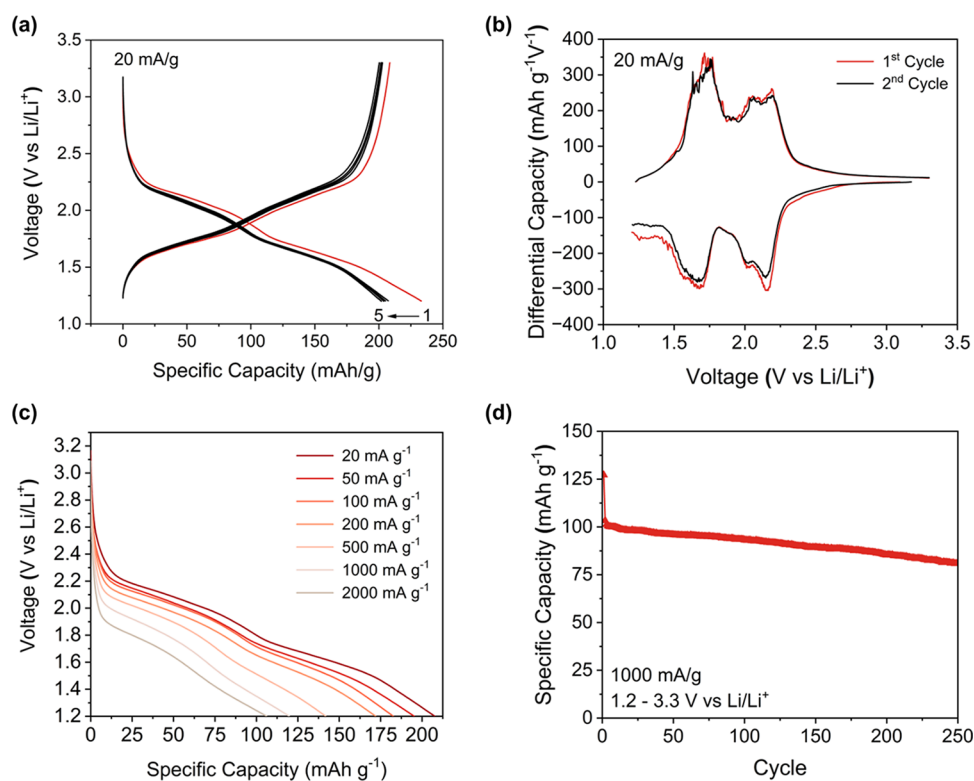
Figure 3. (a) Voltage profiles of $V_7Nb_6O_{29}$ under galvanostatic cycling at 20 mA g^{-1} between 1.2 and 3.3 V for the first five cycles. (b) Differential capacity curve at 20 mA g^{-1} showing two reversible events. (c) Second-cycle rate capability of $V_7Nb_6O_{29}$ at 20, 50, 100, 200, 500, 1000, and 2000 mA g^{-1}. Translated to C-rates, these correspond to approximately C/10, C/4, C/2, C, 2.5C, 5C, and 10C, respectively. (d) Cycling stability at a 1000 mA g^{-1} (~5C) constant charging and discharging rate showing 80% capacity retention after 228 cycles.

The SEM images of the as-synthesized $V_7Nb_6O_{29}$ particles (Figure 2b,c) as well as the particles after shaker milling with carbon black (Figure 2d,e) show that the particle size was reduced from large secondary agglomerates (>15 μm) to primary crystallites and much smaller secondary agglomerates that ranged from 0.5 to 4 μm. X-ray diffraction patterns of the as-prepared and shaker-milled $V_7Nb_6O_{29}$ are provided in Figure S1 and confirm the preservation of the pure $V_7Nb_6O_{29}$ phase. All electrochemical experiments were carried out with this reduced particle size.

Electrochemical testing was performed on $V_7Nb_6O_{29}$ in half-cell format against a Li–metal anode. It is important to note that in a full-cell setup with $V_7Nb_6O_{29}$ as the anode and a

higher-voltage electrode as the cathode (e.g., $LiCoO_2$), lithiation of $V_7Nb_6O_{29}$ would occur during the charging step. By contrast, in a half-cell setup, the lithiation of $V_7Nb_6O_{29}$ would occur during the discharging step. It is for this reason that the half-cell discharge rate performance of $V_7Nb_6O_{29}$ is primarily evaluated. The galvanostatic voltage profiles during Li insertion and extraction are presented in Figure 3a. A second-cycle discharge capacity of 208 mAh/g was observed at a 20 mA/g (~C/10) rate between 1.2–3.3 V and corresponds to roughly 0.8 Li/TM inserted. Note that 1 Li/TM (in total 13 Li/f.u.) would correspond to a theoretical capacity of 253 mAh/g. The capacity drop from the first cycle to the subsequent cycles could result from a combination of factors

including low-voltage side reactions and solid−electrolyte interface formation during the initial discharge as well as irreversible lithium intercalation. Cycling stabilizes significantly from the second cycle onward and is the reason second-cycle capacity is reported. Differential capacity dQ/dV plots of the first two cycles presented in Figure 3b show two primary features involving a nearly equal amount of charge in both the charge and discharge with small polarization. Most capacity is delivered between 1.4−2.4 V with an average discharge voltage of 1.76 V vs Li/Li$^+$, which is relatively low compared with other V-rich ReO$_3$ derivatives, but higher than many other V-free phases.[22,32]

To test the feasibility of this material as an anode in a fast-charging battery, rate capability testing was performed. Each rate was applied on a freshly made coin cell. The second cycle is reported to avoid the irreversible capacity drop associated with the first cycle. The thus obtained data shown in Figure 3c reveals good Li intercalation kinetics. When discharged at 2000 mA/g, it yields a 106 mAh/g capacity in ∼3 min and retains 50.9% of the capacity available at 20 mA/g. Single-cell rate capability testing was also performed and is presented in Figure S2. A standard single-cell rate capability protocol was used that starts at a low rate and progressively cycles at higher rates (cycling the cell three times at each rate) before returning to an intermediate rate to evaluate stability. In this "normal" protocol, we observed negligible capacity at 1000 and 2000 mA/g which stands in stark contrast to the capacities observed in Figure 3c,d. By "inverting" the protocol and starting at high rates, significantly more capacity can be extracted at high rates (∼50 mAh/g at 2000 mA/g and ∼100 mAh/g at 1000 mA/g) without negatively impacting the subsequent low rates. The difference in the observed capacities at high rates is likely the result of different impedance buildup in the two cells. The far less stable cycling at low rates in the "normal" protocol likely causes an impedance buildup that significantly compromises the high-rate performance in the "normal" rate data that is not a concern in the "inverted" rate data. We have also demonstrated good stability over cycling at a 1000 mA g^{-1} (∼5C) constant current charging and discharging rate, achieving 80% capacity retention at 228 cycles (Figure 3d).

To investigate the kinetics of electrochemistry in V$_7$Nb$_6$O$_{29}$, cyclic voltammetry was performed at varying rates from 0.1 to 0.5 mV/s. A well-established relationship between the peak currents and the underlying kinetic mechanism is given by[47]

$$I_p = a\nu^b$$

where ν is the scan rate in mV/s, and a and b are constants. When linearized, the constant b can be extracted and provides insight into the charge storage mechanism of each redox peak, with b = 0.5 corresponding to faradaic behavior with semi-infinite diffusion and b = 1 corresponding to capacitive nondiffusional surface-controlled processes. It is important to note that other early-TM oxide materials also exhibit intermediate b-values which are neither purely capacitive nor purely faradaic.[48] V$_7$Nb$_6$O$_{29}$ has two redox peaks present during both oxidation and reduction. For peaks manifesting as a shoulder, the best approximation of peak position was used. By fitting the power law above to the current of each peak, the b-value for each redox peak can be determined (Figure 4b,c) and are presented as annotations in Figure 4a. The b-values for all redox peaks are between 0.5 and 1, indicating that the electrochemical signature of V$_7$Nb$_6$O$_{29}$ is neither purely
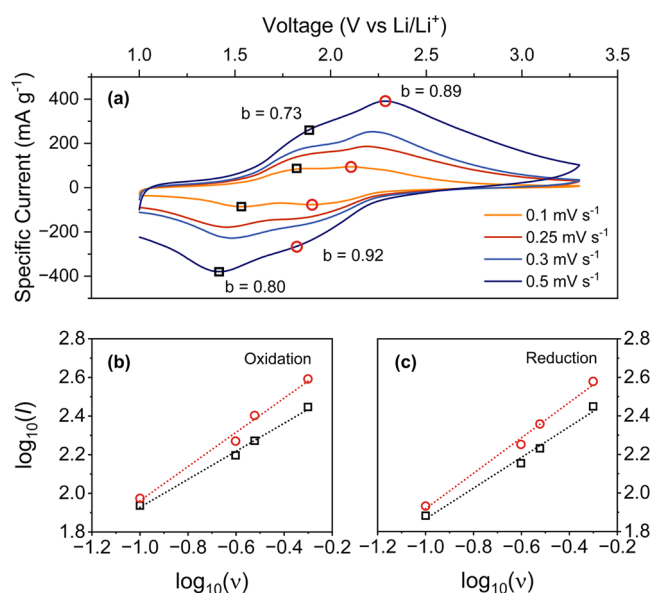

Figure 4. (a) Cyclic voltammetry of V$_7$Nb$_6$O$_{29}$ at varying sweep rates to determine the exponent b value for the different peaks (indicated in the figure). (b, c) Power law linear fits for oxidative and reductive peaks, respectively.

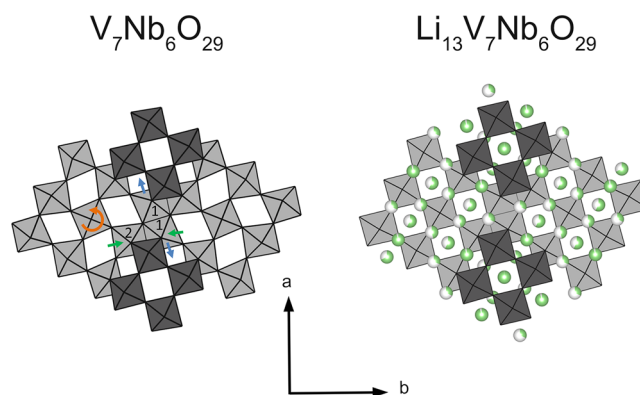capacitive nor purely faradaic, but rather some combination of the two.

Lattice Change during Electrochemical Cycling. XRD was performed on ex situ electrode films that had been cycled to a specific voltage before being disassembled and prepared for diffraction measurements. Six voltages were chosen (1.0, 1.2, 1.9, 2.3, 3.0, and 3.3 V) based on the differential capacity curve (Figure 3b) such that diffraction patterns were measured at the top and bottom voltages as well as immediately outside of clear redox events (Figure 5a). Overall, as indicated by the minimal change among patterns collected on pristine, and at 3.3 V during the first, second, and twentieth cycles, the lattice changes are reversible. Unit cell dimensions were quantified through LeBail fitting of lattice parameters and are presented in Figure 5b. Li intercalation generally expands the unit cell and the lattice changes inside or perpendicular to ab planes are reflected through angle shifts of distinct diffraction peaks. In total, an expansion of approx. 2.2% was observed along the a-axis and 5.8% in the c-axis upon lithiation. Notably, lattice expansion was most significant in the a-axis upon discharge from pristine to 1.9 V, then expansion along the c-axis was predominant once the material was discharged further to 1.2 V, indicating high structural anisotropy. The reverse was observed upon charging. We did not observe the lattice shrink in the ab plane upon intermediate lithiation as in other WR phases,[20] possibly due to the more extensive shear from smaller block sizes in our structure.

Time of flight (TOF) neutron powder diffraction was performed to determine the sites occupied by Li-ions in the fully lithiated state. The Rietveld refinement is shown in Figure 6a, and the associated fit parameters are listed in Table S2. Constraining the refinement to 13 Li per unit cell, we identify 17 Li sites per unit cell that each have some degree of partial occupancy (Figure 6b). In total, eight pocket sites contribute an average of 7.8 Li per unit cell and nine window sites contribute 5.2 Li per unit cell. With the pristine and fully lithiated structures available, we also observed a strong
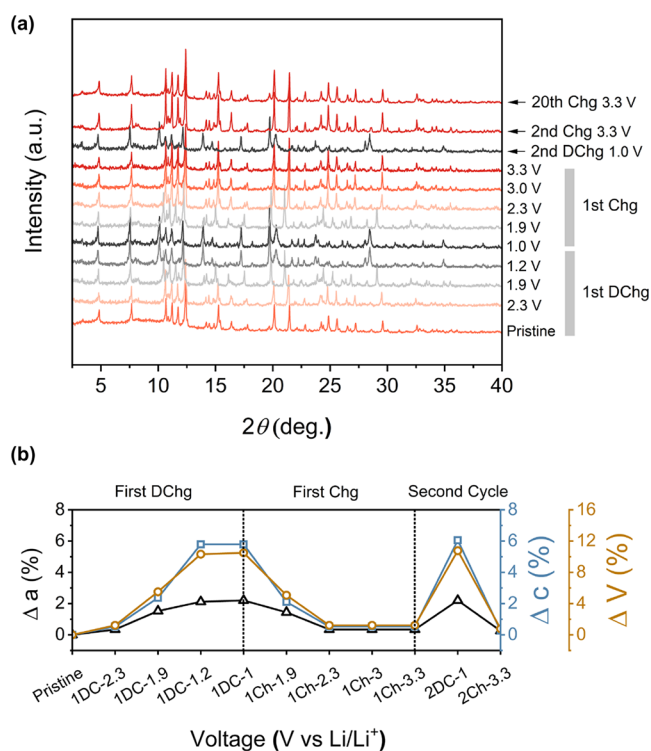
Figure 5. (a) XRD patterns of $V_7Nb_6O_{29}$ films at varying states of charge. Presented, from bottom to top, is the first discharge from pristine to 1.0 V, then the first charge from 1.0 to 3.3 V, the bottom of discharge (1.0 V) and top of charge (3.3 V) for the second cycle followed by the top of charge (3.3 V) of the 20th cycle. (b) Percentage change in lattice parameters a and c and the cell volume based on LeBail fitting on ex situ XRD patterns.


Figure 7. Schematic comparison of the octahedral tilting and distortion in pristine $V_7Nb_6O_{29}$ and lithiated $Li_{13}V_7Nb_6O_{29}$. The central octahedron of the 3×3 block in the pristine structure is rotated 7.2° around the c-axis relative to the block (orange arrow). The distance between two edge-sharing 4k-I sites (labeled "1") is increased and marked with blue arrows. Simultaneously, the distance between 4k-I sites edge-sharing with 4k-II sites (labeled "2") is decreased and marked with green arrows. The addition of 13 Li (green spheres) to the structure reduces the central octahedral tilting.

correlation between octahedral distortion and the degree of tilting, which is most pronounced in the 3×3 block (represented schematically in Figure 7). In its pristine state, the center octahedron of the 3×3 block is tilted 7.2° around the c axis relative to the block. This tilting increases the distance between two edge-sharing 4k-I sites (represented by blue arrows in Figure 7) and reduces the distance between

edge-sharing 4k-I and 4k-II sites (represented by green arrows in Figure 7), leading to large distortion of these octahedra. The octahedral distortion was quantified by the standard deviation (σ) in bond lengths for the 4k-I ($\sigma = 0.1635$ Å) and 4k-II sites ($\sigma = 0.1724$ Å). Upon full lithiation to $Li_{13}V_7Nb_6O_{29}$, the tilting of the center octahedron reduces to 0.6° relative to the orientation of the block and is accompanied by a reduction in the distortion of the 4k-I and 4k-II sites. The standard deviations in bond lengths are lower for both the 4k-I ($\sigma = 0.07658$ Å) and 4k-II sites ($\sigma = 0.1453$ Å) compared with pristine material indicating less distorted octahedra.

A cursory analysis of the Li sites would suggest that each of the features in the differential capacity curve (Figure 3b) corresponds to a type of Li coordination site (pocket or window). However, the features each represent a nearly equal amount of charge and do not match with the approximately 60 and 40% contributions from pockets and windows, respectively. Instead, the order of lithiation is likely much more
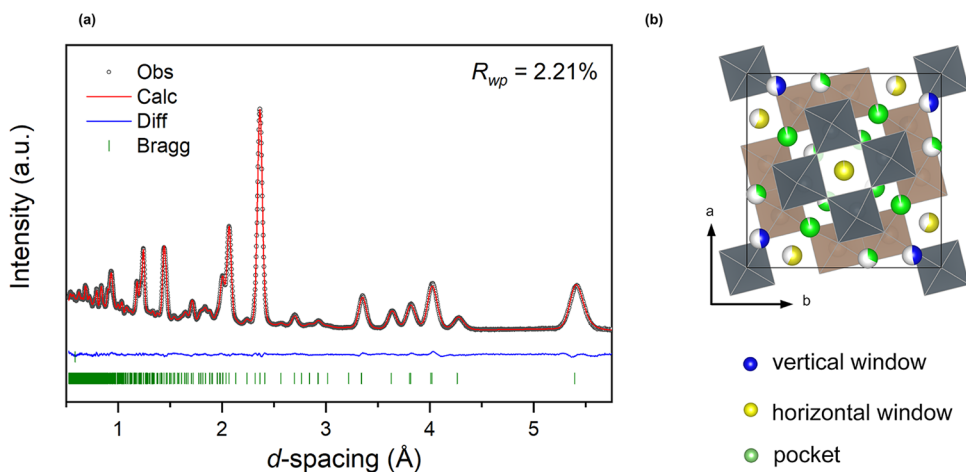
Figure 6. (a) Refinement of TOF powder neutron diffraction data on $Li_{13}V_7Nb_6O_{29}$ collected on NOMAD at room temperature. (b) Schematic representation of fully lithiated $Li_{13}V_7Nb_6O_{29}$ where each colored sphere represents one Li-ion site. All Li-ion sites have partial occupancy, with the fraction of filled sites represented by the fraction of the colored area for each sphere. Vertical and horizontal windows are square-planar coordinated Li-ions with four oxygen ligands. Pockets are square pyramidal Li-ions coordinated by five oxygen ligands.
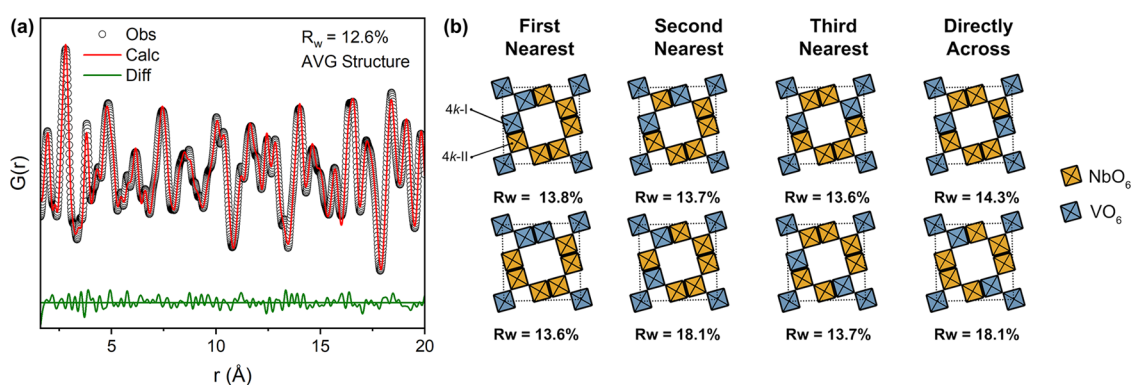
Figure 8. (a) NPDF fitting results based on an average structure. The experimental data are plotted as open black circles, the fitting as a red line, and the difference between observation and calculation as a green line. (b) Schematic representing the eight unique permutations of site ordering in one unit cell. The blue and yellow squares represent VO_6 and NbO_6 octahedra, respectively. For visual clarity, only the 4k sites and their relative position to the V4 2g sites are represented. Site ordering classes (nearest neighbor, second nearest neighbor, third nearest neighbor, and directly across) are defined by terminology that refers to the relative position of the two V ions occupying 4k sites. For each of the site ordering classes, there are two unique permutations. The R_W value obtained from refinement is reported below each schematic representation.
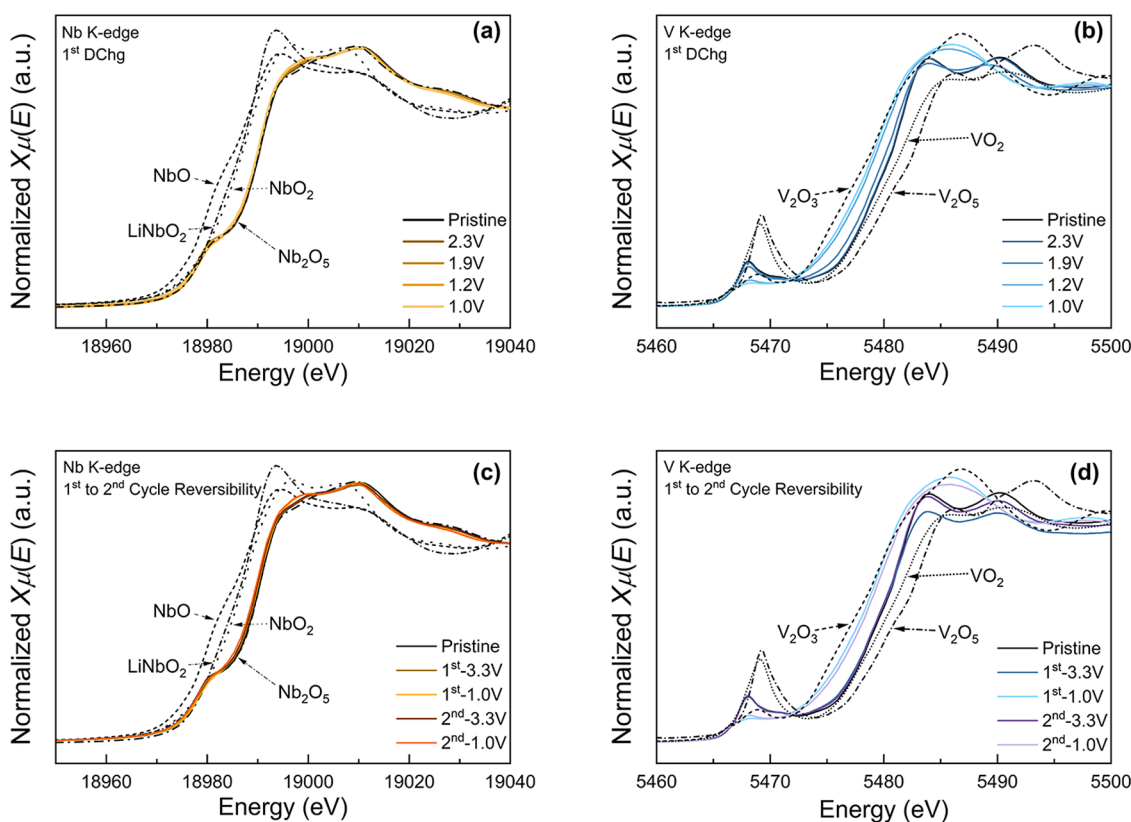

Figure 9. XANES data using (a, c) the Nb K-edge and (b, d) the V K-edge standard. Plots (a) and (b) show the absorption spectra during the first discharge at 2.3, 1.9, 1.2, and 1.0 V. Plots (c) and (d) show the reversibility of oxidation state change by comparing absorption spectra at the lower and upper cutoff voltages across the first two cycles.

complex, as is common with many other WR phase materials. Both DFT[22] and combined DFT/diffraction[32] studies have demonstrated that, while pockets are generally lower-energy Li sites, the relative energetics of various Li sites change greatly during lithiation, with certain window sites being lower in energy than some pocket sites at certain states of charge. A similarly complex order of lithiation is likely present in $V_7Nb_6O_{29}$.

Local-Structure Characterization. The starting parameters for NPDF refinement in a short interatomic distance range (1.6–20 Å) were obtained from the single-crystal X-ray

structural refinement. The absorption coefficient averaged over the entire wavelength range of the TOF neutron data was obtained from Rietveld refinement and is quite minimal, 0.049 cm^{-1} (refinement results in Figure S3 and Table S3). When the average structural model with $P4/m$ space group type was used, we obtained a reasonable R_W = 12.6% by refining lattice parameters, occupancies in the two V/Nb mixed 4k Wyckoff sites, isotropic thermal parameters, peak shape factor δ_1, and instrument parameters Q_{damp} and Q_{broad}. The refined NPDF parameters are presented in Table S4. The data is presented in Figure 8a, which shows minor deviations between observation
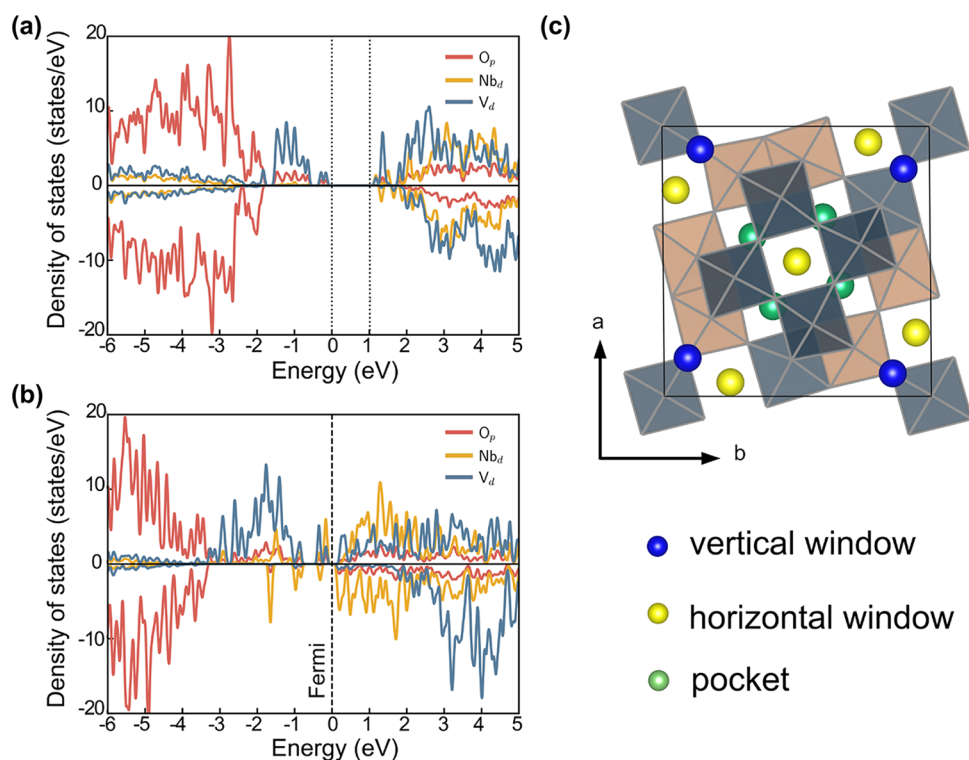
Figure 10. Electronic density of states calculations for (a) unlithiated and (b) fully lithiated structures. (c) Schematic representation of the fully lithiated $Li_{13}V_7Nb_6O_{29}$ used for DFT calculations where each colored sphere represents one Li-ion site with full occupancy. Vertical and horizontal windows are square-planar coordinated Li-ions with four oxygen ligands. Pockets are square pyramidal Li-ions coordinated by five oxygen ligands.

and calculations without missing any major features. The refined occupancies in the two mixed 4k sites are very close to the values obtained from high-resolution neutron diffraction refinement from a different beamline. The first site was refined to 84.7% Nb and 15.3% V occupancy, and the second site was refined to 62.1% Nb and 37.9% V occupancy. This indicates excellent accuracy of our structural determination, which likely benefited from the drastically different neutron scattering lengths of V and Nb.

We then explored more sophisticated structural modifications with short-range substitutional order between V and Nb in the two 4k Wyckoff positions (in total 8 sites within one unit cell) to identify favorable ordering configurations. Because the refinement of neutron diffraction and NPDF data indicates close to 75% Nb and 25% V in these sites, they are occupied by an average of 6 Nb and 2 V atoms per unit cell, presenting 28 arrangement possibilities. Upon consideration of the fourfold rotational symmetry of the structure, the number drops to only 8 permutations as shown in Figure 8b. Based on the parameters obtained from refining the average structure, we then modified the structural model with these 8 arrangements for a few more iterations and the final R_W values are also reported in Figure 8b.

Based on the PDF refinement, none of the individual site ordering possibilities have R_w values lower than the average structure refinement. Although some permutations of site ordering refine slightly better than others, it is clear that no single site-ordering permutation is dominant and that the actual local structure is likely a statistical distribution of multiple configurations. Such site substitutional disorder will cause a dispersive distribution of Li site energy, which likely contributes to the overall sloping voltage profiles observed. For simplicity, one of the best-fitting configurations, the lower one

in the "third nearest" column of Figure 8b, was then used for DFT calculations and analysis.

Redox Mechanism. Ex situ XANES was performed to understand the redox mechanism of $V_7Nb_6O_{29}$ during Li intercalation and extraction. Figure 9a,b shows Nb and V K-edge spectra, respectively. The various states of charge during the first discharge were selected immediately before and after the hump features shown in the differential capacity curve (Figure 3b). Figure 9c,d plots the spectra upon full discharge/charge for the first two cycles. The pristine $V_7Nb_6O_{29}$ spectra indicate that the oxidation states on Nb and V are 5+ and 4+, respectively, agreeing with our expectations. At the Nb K-edge (Figure 9a,c), the absorption spectra nearly superimpose over the Nb_2O_5 standard for all states of charge during both charging and discharging, indicating that Nb has limited redox activity and maintains an oxidation state close to 5+.

In contrast, absorption at the V K-edge (Figure 9b) demonstrates V reduction throughout the entire voltage window. The edge position starts in the vicinity of VO_2, indicating a 4+ initial oxidation state, and continuously shifts to lower energy at 1.9, 1.2, and 1.0 V. Toward the end of discharge, at 1.2 V and below, we find that the V^{3+}/V^{2+} couple is also present. One of the earliest XANES studies on V-oxides by Wong et al. demonstrated that the edges of VO and V_2O_3 are in nearly the same position and that the largest difference arises in the pre-edge peak.[49] This pre-edge peak is strong in the V_2O_5 and VO_2 standards and is attributed to the 1s → 3d transition that is possible due to tetrahedral or distorted octahedral coordination environments in V_2O_5 and VO_2, respectively.[49,50] Coordination environments are more symmetrical in V_2O_3 and VO; however, VO is the most symmetrical of the two. Thus, the pre-edge feature that is only weakly present in V_2O_3 nearly disappears in VO. This

behavior is well reflected in the data as the pre-edge at 1.2 V is already weaker than that of the V_2O_3 standard and nearly disappears at 1.0 V, which reinforces the conclusion that the V^{3+}/V^{2+} couple is present. Note that in the entire voltage range, the pre-edge feature remains low in intensity, suggesting reduced distortion in V coordination environment and stable VO_6 octahedra during Li insertion and extraction. After the first discharge, as the sample is charged back to 3.3 V and undergoes a second cycle, the pre-edge feature restores, indicating that the evolution of V coordination environments is fully reversible in this material (Figure 9d), which might explain the smaller irreversible capacity in $V_7Nb_6O_{29}$ compared to other V-based ReO_3-derivative anodes.[32] The edge and pre-peak shifts seen in the XANES data do not show a one-to-one correspondence between TM redox couples and the two redox peaks observed in the differential capacity curve (Figure 3b) and cyclic voltammetry (Figure 4a). Therefore, we speculate that the hump features in electrochemical dQ/dV data originate from the sequential lithiation of sites with complex and highly variable site energies.[22,32]

To understand the electronic structure of $V_7Nb_6O_{29}$ before and after lithiation as well as the orbitals involved in realizing the observed redox, DFT calculations were carried out based on a reasonably refined structural model from NPDF (Figure 8b, the third from left in the lower row). A band gap of ~1 eV is predicted for the empty $V_7Nb_6O_{29}$ framework based on the electronic density of states (DOS, Figure 10a), which is likely due to the structural distortion as well as electron-electron repulsion and agrees with the observed black color of the as-synthesized powder. The valence band is primarily composed of filled O 2p and V 3d orbitals, consistent with the d^1 electronic configuration of V^{4+}, while the conduction band is mainly composed of the empty d orbitals of V and Nb. The lowest unoccupied states have a much larger contribution from V than Nb, suggesting that with a rigid band approximation, V states will accept more electrons and provide more redox capacity upon lithiation. Given the complex Li-vacancy ordering possibilities at intermediate lithiation levels, only the fully lithiated structure of $Li_{13}V_7Nb_6O_{29}$ is computationally investigated and its electronic DOS plot is shown in Figure 10b. Electrochemical powder lithiation of $V_7Nb_6O_{29}$ at low current density with yielded constant voltage trickle discharge yielded ~250 mAh/g capacity, nearly precisely the capacity expected for 1 Li/TM (253 mAh/g). The structure for $Li_{13}V_7Nb_6O_{29}$ DFT calculations was generated by assigning full occupation of a subset of the Li sites that were observed through TOF neutron diffraction (Figure 6) such that a total of 13 Li/f.u. were contributed. These sites (labeled in Figure 10c and tabulated in Table S5) include nine 4-coordinated square-planar window sites (eight in the 3 × 3 blocks with four lying vertically and four horizontally, as well as one lying horizontally in the 2 × 2 blocks) and four 5-coordinated square pyramidal pocket sites between a 2 × 2 block and its nearby 3 × 3 blocks. Since WR phases typically undergo an insulator-to-metal transition during lithiation, electrons are not localized around the occupied Li sites and we expect the computational output to be independent of the specific Li sites chosen for DFT. This lithiated structure was then computationally relaxed to extract the DOS. Any deviation from this configuration might affect the formation energy but this structure should already provide a reasonably accurate prediction of the final metal valences given the largely itinerary nature of electrons in heavily n-doped Wadsley−Roth phases.[22] The resulting

oxidation states of Nb and V after 13 Li/f.u. intercalation are +4.67 and +2.43, respectively, indicating merely 15% of the capacity from Nb redox and the rest 85% from V redox. This is consistent with the minimal edge shift observed in the Nb XANES as well as the diminished pre-edge feature for a lower than +3 oxidation state in the V XANES.

■ DISCUSSION

WR shear phases have been known to adopt cation-disordered structures when two or more transition-metal species are present.[21,22,51,52] Since metal−metal distances are larger in the center octahedra of the ReO_3-type blocks, simple electrostatics would indicate that these sites should be preferentially occupied by the more oxidized species.[22,53] Cation sites at the block periphery share edges with nearby blocks and tend to be occupied by less oxidized species. Indeed, previous computational and experimental results have demonstrated such cation site preferences which minimize structural distortion from electrostatic repulsion. Note that super-structures and short-range ordering of cation distributions are necessary to properly describe the observed partial occupancies at each metal site.[22,53]

However, the TM occupancy in $V_7Nb_6O_{29}$ does not follow this general trend that is based on pure electrostatics.[54] The higher-valent Nb^{5+} occupies the periphery sites of the 3 × 3 blocks, leaving the center site to be solely V^{4+}-occupied. To better understand the occupation preferences of Nb and V, BVS[55] analysis was performed based on the bond lengths depicted in Figure 1c. The results are tabulated in Table 4. The

Table 4. Bond Valence Sum of V^{4+} and Nb^{5+} for Each Unique TM Site

	bond valence sum	
	V^{4+}	Nb^{5+}
4k-I site (Nb1/V1)	3.65	5.14
4k-II site (Nb2/V2)	3.68	5.19
4j site (V3)	4.15	5.05
2g site (V4)	4.17 (with splitting)	5.88 (with splitting)
	4.30 (without splitting)	6.05 (without splitting)

most significant deviation from ionic formal oxidation states is observed for V^{4+} in both the 4k-I and 4k-II sites as well as for Nb^{5+} in the 2g site. These site preferences likely dictate Nb occupation priority in the 4k sites as well as exclusive V occupancy in the 2g site. Occupation in the 4k sites is then brought to unity by filling with V. Finally, the remaining V fills (and exclusively occupies) the 4j site. The BVS deviation for V^{4+} in the 4k-I site is also more significant than in the 4k-II site, which might explain the different Nb/V mixing ratios in these two sites.

Furthermore, BVS justifies the V-position splitting along the z-axis in the 2g site. For that metal site, the BVS deviation from the formal oxidation state of V^{4+} is reduced when the site is split. On the other hand, whether with or without splitting, the BVS is much larger than the formal oxidation state of Nb^{5+}, which explains why Nb is excluded from occupying this site. Given the extensive shear in the structure, i.e., the 2 × 2 blocks and the 8 periphery sites of the 3 × 3 blocks are all sheared, the size of the center metal site (2g site) in the 3 × 3 block is dictated by this very stiff, sheared framework and is too small for a Nb^{5+} ion. Note that in the ICSD, only one compound, $V_{2.38}Nb_{10.7}O_{32.7}$,[56] has been reported that contains off-center

split Nb sites, whereas dozens of ternary V-containing oxides are reported with V site splitting (many along the V–O direction). This implies that V is much more prone to off-center splitting than Nb, possibly due to the complex electronic or magnetic ground states of V^{4+}, such as in $Sr_2V_3O_9$.[57]

Our XANES results indicate minimal Nb reduction even upon full lithiation, which agrees with DFT calculations. Based on DFT, the final Nb valence in $Li_{13}V_7Nb_6O_{29}$ should be roughly +4.67. The accompanying Nb K-edge shift, though minimal, is comparable to literature results on WR anodes at similar valence changes. For example, the WR phase $Nb_{16}W_5O_{55}$ at 0.3 Li/TM lithiation (corresponding to $Li_{6.3}Nb_{16}W_5O_{55}$) was expected to have a Nb oxidation state of roughly +4.72,[20] and its Nb K-edge shift between pristine and this partially lithiated state was estimated to be ~0.57 eV based on the peak shift in the first derivative of the absorption spectrum. Taking the first derivative on our XANES data (Figure S4) of the pristine and the fully discharged compound yields a peak shift of ~0.71 eV, close to the literature observation.

The lack of Nb redox is unusual for Nb-containing Wadsley–Roth phases. We speculate that the octahedral distortion in this heavily sheared structure might have caused the unusually small Nb reduction. The standard reduction potentials should otherwise follow the order of V^{4+}/V^{3+} = 0.337 V,[58] Nb^{5+}/Nb^{4+} = −0.06 V,[59] V^{3+}/V^{2+} = −0.255 V[60] (vs SHE). However, based on DFT computations in the literature,[32] the order of electron filling is strongly affected by the octahedral distortion. In a perfect octahedral coordination environment, both V and Nb d orbitals split into t_{2g} and e_g orbitals. Any distortion to the octahedron can cause the degenerate t_{2g} orbitals to further split. For example, in PNb_9O_{25}, the t_{2g} nonbonding orbitals of the Nb^{5+} ions in the distortion-free block-center sites are occupied first, followed by the hybridized t_{2g} orbitals of the Nb^{5+} ions in the highly distorted block-periphery sites. We observed very strong octahedral distortion in $V_7Nb_6O_{29}$, as shown in updated Figure 1, likely because 12 out of the 13 total metal sites in the structure are edge-sharing with neighbors. It is possible that the distinct distortion in the NbO_6 and VO_6 octahedra lead to different orbital splitting, causing the reversal and overlap in the reduction order of Nb^{5+}/Nb^{4+} and V^{3+}/V^{2+}.

Our discovery of $V_7Nb_6O_{29}$ as a potential Li-ion anode material provides an excellent example in which considerable redox capacity is mainly provided by V, a more earth-abundant and lighter element than Nb. The average operating voltage is +1.76 V vs Li/Li^+, which is lower than the V^{5+}-containing ReO_3-derivative phases that have been reported in the past.[34,35] Furthermore, V^{4+} and its reduced states are all stable in octahedral coordination to facilitate highly reversible valence change. The Nb, though providing limited redox, is critical for creating the many Li intercalation sites. In ReO_3-derivative phases, crystallographic shear can be controlled by tuning the ratio of transition-metal ions to the number of oxygen ligands, TM/O. More shear forms as the average TM valence decreases and the ratio of TM/O increases, causing a denser structure with fewer Li intercalation sites. Since our structure has V in its low 4+ oxidation state, the higher-valent Nb keeps the overall TM/O ratio low, increasing the theoretical Li site capacity of the material.

CONCLUSIONS

In this work, we reported the structural and electrochemical characterization of $V_7Nb_6O_{29}$, a new V-rich Wadsley–Roth shear phase with promise as an anode for Li-ion batteries. Initially discovered as a byproduct of chemical vapor transport, the structure was unambiguously solved using single-crystal X-ray diffraction refinement and was shown to have $2 \times 2 \times \infty$ and $3 \times 3 \times \infty$ octahedra blocks with open channels that extend one-dimensionally. Electrochemical characterization showed that these channels are open to Li diffusion, allowing $V_7Nb_6O_{29}$, to achieve excellent rate capability and ~208 mAh/g specific capacity with an average voltage of +1.76 V vs Li/Li^+. Neutron pair distribution function analysis revealed that transition-metal disorder is most favorably accounted for through partial V occupancy preferably in the more edge-shared 4k site. These insights combined with X-ray absorption spectroscopy and density functional theory calculations showed that V redox accounts for the majority of the observed capacity. Furthermore, the stable octahedral coordination adopted by V^{4+} in the material contributes to cycling stability, while Nb^{5+} keeps the overall TM/O ratio low to increase the theoretical Li site capacity. This study represents a step forward in demonstrating good electrochemical performance in V-rich anodes for Li-ion batteries.

ASSOCIATED CONTENT

SI Supporting Information

The Supporting Information is available free of charge at https://pubs.acs.org/doi/10.1021/acs.chemmater.2c03465.

> Crystallographic information files (CIF) for all structural determinations, raw BVSE isosurface (.CUBE file) (ZIP) XRD comparison of as-synthesized and shaker-milled $V_7Nb_6O_{29}$; single-cell rate capability data; refinement of TOF powder neutron diffraction data on $V_7Nb_6O_{29}$ collected on NOMAD at room temperature; differentiated Nb K-edge absorption data comparison of pristine and lithiated material; constant-wavelength neutron diffraction atomic sites; TOF neutron diffraction (pristine and lithiated) and PDF atomic sites; and Li sites used for DFT band structure calculations (PDF)

AUTHOR INFORMATION

Corresponding Authors

Jared M. Allred − Department of Chemistry and Biochemistry, University of Alabama, Tuscaloosa, Alabama 35487, United States; ⊙ orcid.org/0000-0002-5953-300X; Email: jmallred@ua.edu

Huiwen Ji − Department of Materials Science & Engineering, University of Utah, Salt Lake City, Utah 84112, United States; Email: huiwen.ji@utah.edu

Authors

Erick A. Lawrence − Department of Materials Science & Engineering, University of Utah, Salt Lake City, Utah 84112, United States; ⊙ orcid.org/0000-0003-0819-1895

Matthew A. Davenport − Department of Chemistry and Biochemistry, University of Alabama, Tuscaloosa, Alabama 35487, United States

Reshma Devi − Department of Materials Engineering, Indian Institute of Science, Bengaluru 560012 Karnataka, India

Zijian Cai − Department of Materials Science and Engineering, University of California Berkeley, Berkeley, California 94720,

United States; Materials Sciences Division, Lawrence Berkeley National Laboratory, Berkeley, California 94720, United States; orcid.org/0000-0002-4908-3180

Maxim Avdeev − *Australian Centre for Neutron Scattering, Australian Nuclear Science and Technology Organization, Sydney, New South Wales 2232, Australia; School of Chemistry, University of Sydney, Sydney, New South Wales 2006, Australia;* orcid.org/0000-0003-2366-5809

Jonathan R. Belnap − *Department of Materials Science & Engineering, University of Utah, Salt Lake City, Utah 84112, United States*

Jue Liu − *Neutron Sciences Division, Oak Ridge National Laboratory, Oak Ridge, Tennessee 37831, United States;* orcid.org/0000-0002-4453-910X

Husain Alnaser − *Department of Materials Science & Engineering, University of Utah, Salt Lake City, Utah 84112, United States*

Alice Ho − *Department of Materials Science and Engineering, Carnegie Mellon University, Pittsburgh, Pennsylvania 15213, United States*

Taylor D. Sparks − *Department of Materials Science & Engineering, University of Utah, Salt Lake City, Utah 84112, United States;* orcid.org/0000-0001-8020-7711

Gopalakrishnan Sai Gautam − *Department of Materials Engineering, Indian Institute of Science, Bengaluru 560012 Karnataka, India;* orcid.org/0000-0002-1303-0976

Complete contact information is available at:
https://pubs.acs.org/10.1021/acs.chemmater.2c03465

Notes
The authors declare no competing financial interest.

◼ REFERENCES

(1) Lithium-ion Battery Market Size Worth $182.53 Billion By 2030: Grand View Research, Inc, 2022. https://www.bloomberg.com/press-releases/2022-06-07/lithium-ion-battery-market-size-worth-182-53-billion-by-2030-grand-view-research-inc. (accessed January 09, 2022).

(2) Downie, L. E.; Krause, L.; Burns, J.; Jensen, L.; Chevrier, V.; Dahn, J. In situ detection of lithium plating on graphite electrodes by electrochemical calorimetry. *J. Electrochem. Soc.* **2013**, *160*, A588−A594.

(3) Lu, W.; López, C. M.; Liu, N.; Vaughey, J. T.; Jansen, A.; Dennis, W. D. Overcharge effect on morphology and structure of carbon electrodes for lithium-ion batteries. *J. Electrochem. Soc.* **2012**, *159*, A566−A570.

(4) Shen, C.; Hu, G.; Cheong, L. Z.; Huang, S.; Zhang, J. G.; Wang, D. Direct observation of the growth of lithium dendrites on graphite anodes by operando EC-AFM. *Small Methods* **2018**, *2*, No. 1700298.

(5) Aurbach, D.; Zinigrad, E.; Cohen, Y.; Teller, H. A short review of failure mechanisms of lithium metal and lithiated graphite anodes in liquid electrolyte solutions. *Solid State Ionics* **2002**, *148*, 405−416.

(6) Ferg, E.; Gummow, R. J.; De Kock, A.; Thackeray, M. Spinel anodes for lithium-ion batteries. *J. Electrochem. Soc.* **1994**, *141*, L147−L150.

(7) Ohzuku, T.; Ueda, A.; Yamamoto, N. Zero-strain insertion material of Li [Li1/3Ti5/3] O 4 for rechargeable lithium cells. *J. Electrochem. Soc.* **1995**, *142*, 1431−1435.

(8) Julien, C.; Zaghib, K. Electrochemistry and local structure of nano-sized Li4/3Me5/3O4 (MeMn, Ti) spinels. *Electrochim. Acta* **2004**, *50*, 411−416.

(9) Wang, G.; Bradhurst, D.; Dou, S.; Liu, H. Spinel Li [Li1/3Ti5/3] O 4 as an anode material for lithium ion batteries. *J. Power Sources* **1999**, *83*, 156−161.

(10) Komaba, S.; Ozeki, T.; Okushi, K. Functional interface of polymer modified graphite anode. *J. Power Sources* **2009**, *189*, 197−203.

(11) Peled, E.; Menachem, C.; Bar-Tow, D.; Melman, A. Improved graphite anode for lithium-ion batteries chemically: Bonded solid electrolyte interface and nanochannel formation. *J. Electrochem. Soc.* **1996**, *143*, L4−L7.

(12) Chen, K.; Yang, H.; Liang, F.; Xue, D. Microwave-irradiation-assisted combustion toward modified graphite as lithium ion battery anode. *ACS Appl. Mater. Interfaces* **2018**, *10*, 909−914.

(13) Wang, X.; Yan, C.; Yan, J.; Sumboja, A.; Lee, P. S. Orthorhombic niobium oxide nanowires for next generation hybrid supercapacitor device. *Nano Energy* **2015**, *11*, 765−772.

(14) Wei, M.; Wei, K.; Ichihara, M.; Zhou, H. Nb2O5 nanobelts: a lithium intercalation host with large capacity and high rate capability. *Electrochem. Commun.* **2008**, *10*, 980−983.

(15) Come, J.; Augustyn, V.; Kim, J. W.; Rozier, P.; Taberna, P.-L.; Gogotsi, P.; Long, J. W.; Dunn, B.; Simon, P. Electrochemical kinetics of nanostructured Nb2O5 electrodes. *J. Electrochem. Soc.* **2014**, *161*, A718−A725.

(16) Kim, J. W.; Augustyn, V.; Dunn, B. The effect of crystallinity on the rapid pseudocapacitive response of Nb2O5. *Adv. Energy Mater.* **2012**, *2*, 141−148.

(17) Ren, Y.; Liu, Z.; Pourpoint, F.; Armstrong, A. R.; Grey, C. P.; Bruce, P. G. Nanoparticulate TiO2 (B): an anode for lithium-ion batteries. *Angew. Chem.* **2012**, *124*, 2206−2209.

(18) Hibino, M.; Abe, K.; Mochizuki, M.; Miyayama, M. Amorphous titanium oxide electrode for high-rate discharge and charge. *J. Power Sources* **2004**, *126*, 139−143.

(19) Xu, J.; Jia, C.; Cao, B.; Zhang, W. Electrochemical properties of anatase TiO2 nanotubes as an anode material for lithium-ion batteries. *Electrochim. Acta* **2007**, *52*, 8044−8047.

(20) Griffith, K. J.; Wiaderek, K. M.; Cibin, G.; Marbella, L. E.; Grey, C. P. Niobium tungsten oxides for high-rate lithium-ion energy storage. *Nature* **2018**, *559*, 556−563.

(21) Griffith, K. J.; Grey, C. P. Superionic lithium intercalation through 2 × 2 nm2 columns in the crystallographic shear phase Nb18W8O69. *Chem. Mater.* **2020**, *32*, 3860−3868.

(22) Koçer, C. P.; Griffith, K. J.; Grey, C. P.; Morris, A. J. Cation disorder and lithium insertion mechanism of Wadsley−Roth crystallographic shear phases from first principles. *J. Am. Chem. Soc.* **2019**, *141*, 15121−15134.

(23) Cava, R. J.; Santoro, A.; Murphy, D.; Zahurak, S.; Roth, R. Structural aspects of lithium insertion in oxides: LixReO3 and Li2FeV3O8. *Solid State Ionics* **1981**, *5*, 323−326.

(24) Cava, R.; Santoro, A.; Murphy, D.; Zahurak, S.; Roth, R. The structures of lithium-inserted metal oxides: LiReO3 and Li2ReO3. *J. Solid State Chem.* **1982**, *42*, 251−262.

(25) Cava, R. J.; Murphy, D.; Zahurak, S. Lithium insertion in Wadsley-Roth phases based on niobium oxide. *J. Electrochem. Soc.* **1983**, *130*, 2345−2351.

(26) Liu, H.; Zhu, Z.; Yan, Q.; Yu, S.; He, X.; Chen, Y.; Zhang, R.; Ma, L.; Liu, T.; Li, M.; et al. A disordered rock salt anode for fast-charging lithium-ion batteries. *Nature* **2020**, *585*, 63−67.

(27) Vincent, R. C.; Luo, Y.; Andrews, J. L.; Zohar, A.; Zhou, Y.; Yan, Q.; Mozur, E. M.; Preefer, M. B.; Weker, J. N.; Cheetham, A. K.; et al. High-Rate Lithium Cycling and Structure Evolution in Mo4O11. *Chem. Mater.* **2022**, *34*, 4122−4133.

(28) Griffith, K. J.; Seymour, I. D.; Hope, M. A.; Butala, M. M.; Lamontagne, L. K.; Preefer, M. B.; Koçer, C. P.; Henkelman, G.; Morris, A. J.; Cliffe, M. J.; et al. Ionic and electronic conduction in TiNb2O7. *J. Am. Chem. Soc.* **2019**, *141*, 16706−16725.

(29) Bashian, N. H.; Preefer, M. B.; Milam-Guerrero, J.; Zak, J. J.; Sendi, C.; Ahsan, S. A.; Vincent, R. C.; Haiges, R.; See, K. A.; Seshadri, R.; Melot, B. C. Understanding the role of crystallographic shear on the electrochemical behavior of niobium oxyfluorides. *J. Mater. Chem. A* **2020**, *8*, 12623−12632.

(30) Reddy, M.; Madhavi, S.; Rao, G. S.; Chowdari, B. Metal oxyfluorides TiOF2 and NbO2F as anodes for Li-ion batteries. *J. Power Sources* **2006**, *162*, 1312−1321.

(31) Griffith, K. J.; Forse, A. C.; Griffin, J. M.; Grey, C. P. High-rate intercalation without nanostructuring in metastable Nb2O5 bronze phases. *J. Am. Chem. Soc.* **2016**, *138*, 8888−8899.

(32) Saber, M.; Preefer, M. B.; Kolli, S. K.; Zhang, W.; Laurita, G.; Dunn, B.; Seshadri, R.; Van der Ven, A. Role of Electronic Structure in Li Ordering and Chemical Strain in the Fast Charging Wadsley−Roth Phase PNb9O25. *Chem. Mater.* **2021**, *33*, 7755−7766.

(33) Gaultois, M. W.; Sparks, T. D.; Borg, C. K.; Seshadri, R.; Bonificio, W. D.; Clarke, D. R. Data-driven review of thermoelectric materials: performance and resource considerations. *Chem. Mater.* **2013**, *25*, 2911−2920.

(34) Murphy, D. W.; Christian, P. Solid state electrodes for high energy batteries. *Science* **1979**, *205*, 651−656.

(35) Wyckoff, K. E.; Robertson, D. D.; Preefer, M. B.; Teicher, S. M.; Bienz, J.; Kautzsch, L.; Mates, T. E.; Cooley, J. A.; Tolbert, S. H.; Seshadri, R. High-Capacity Li+ Storage through Multielectron Redox in the Fast-Charging Wadsley−Roth Phase (W0. 2V0. 8) 3O7. *Chem. Mater.* **2020**, *32*, 9415−9424.

(36) Preefer, M. B.; Saber, M.; Wei, Q.; Bashian, N. H.; Bocarsly, J. D.; Zhang, W.; Lee, G.; Milam-Guerrero, J.; Howard, E. S.; Vincent, R. C.; et al. Multielectron redox and insulator-to-metal transition upon lithium insertion in the fast-charging, Wadsley−Roth phase PNb9O25. *Chem. Mater.* **2020**, *32*, 4553−4563.

(37) Sheldrick, G. M. A short history of SHELX. *Acta Crystallogr., Sect. A: Found. Crystallogr.* **2008**, *64*, 112−122.

(38) Farrugia, L. J. WinGX and ORTEP for Windows: an update. *J. Appl. Crystallogr.* **2012**, *45*, 849−854.

(39) Momma, K.; Izumi, F. VESTA: a three-dimensional visualization system for electronic and structural analysis. *J. Appl. Crystallogr.* **2008**, *41*, 653−658.

(40) Avdeev, M.; Hester, J. R. ECHIDNA: a decade of high-resolution neutron powder diffraction at OPAL. *J. Appl. Crystallogr.* **2018**, *51*, 1597−1604.

(41) Larson, A. C.; Von Dreele, R. B. *Gsas*, Report IAUR, 1994; 86−748.

(42) Toby, B. H. EXPGUI, a graphical user interface for GSAS. *J. Appl. Crystallogr.* **2001**, *34*, 210−213.

(43) Farrow, C. L.; Juhas, P.; Liu, J.; Bryndin, D.; Božin, E.; Bloch, J.; Proffen, T.; Billinge, S. PDFfit2 and PDFgui: computer programs for studying nanostructure in crystals. *J. Phys.: Condens. Matter* **2007**, *19*, No. 335219.

(44) Toby, B. H.; Von Dreele, R. B. GSAS-II: the genesis of a modern open-source all purpose crystallography software package. *J. Appl. Crystallogr.* **2013**, *46*, 544−549.

(45) Ravel, B.; Newville, M. ATHENA, ARTEMIS, HEPHAESTUS: data analysis for X-ray absorption spectroscopy using IFEFFIT. *J. Synchrotron Radiat.* **2005**, *12*, 537−541.

(46) Chen, H.; Wong, L. L.; Adams, S. SoftBV−a software tool for screening the materials genome of inorganic fast ion conductors. *Acta Crystallogr., Sect. B: Struct. Sci., Cryst. Eng. Mater.* **2019**, *75*, 18−33.

(47) Lindström, H.; Södergren, S.; Solbrand, A.; Rensmo, H.; Hjelm, J.; Hagfeldt, A.; Lindquist, S.-E. Li+ ion insertion in TiO2 (anatase). 2. Voltammetry on nanoporous films. *J. Phys. Chem. B* **1997**, *101*, 7717−7722.

(48) Mathis, T. S.; Kurra, N.; Wang, X.; Pinto, D.; Simon, P.; Gogotsi, Y. Energy storage data reporting in perspective-guidelines for interpreting the performance of electrochemical energy storage systems. *Adv. Energy Mater.* **2019**, *9*, No. 1902007.

(49) Wong, J.; Lytle, F.; Messmer, R.; Maylotte, D. K-edge absorption spectra of selected vanadium compounds. *Phys. Rev. B* **1984**, *30*, 5596−5610.

(50) Sutton, S.; Karner, J.; Papike, J.; Delaney, J.; Shearer, C.; Newville, M.; Eng, P.; Rivers, M.; Dyar, M. Vanadium K edge XANES of synthetic and natural basaltic glasses and application to microscale oxygen barometry. *Geochim. Cosmochim. Acta* **2005**, *69*, 2333−2348.

(51) Voskanyan, A. A.; Abramchuk, M.; Navrotsky, A. Entropy stabilization of TiO2−Nb2O5 Wadsley−Roth shear phases and their prospects for lithium-ion battery anode materials. *Chem. Mater.* **2020**, *32*, 5301−5308.

(52) Lv, Z.; Zhu, H.; Meng, W.; Wei, L.; Yang, Y.; Zhang, Y.; Ye, M.; Li, C. C. Cation mixing in Wadsley-Roth phase anode of lithium-ion battery improves cycling stability and fast Li+ storage. *Appl. Phys. Rev.* **2021**, *8*, No. 031404.

(53) Cheetham, A. K.; Von Dreele, R. Cation distributions in niobium oxide block structures. *Nat. Phys. Sci.* **1973**, *244*, 139−140.

(54) Urban, A.; Abdellahi, A.; Dacek, S.; Artrith, N.; Ceder, G. Electronic-structure origin of cation disorder in transition-metal oxides. *Phys. Rev. Lett.* **2017**, *119*, No. 176402.

(55) Brown, I. D. Bond valences-A simple structural model for inorganic chemistry. *Chem. Soc. Rev.* **1978**, *7*, 359−376.

(56) Börrnert, C.; Carrillo-Cabrera, W.; Simon, P.; Langbein, H. V2. 38Nb10. 7O32. 7: A V2O5−Nb2O5 mixed oxide tunnel structure related to the tetragonal tungsten bronzes. *J. Solid State Chem.* **2010**, *183*, 1038−1045.

(57) Ivanshin, V. A.; Yushankhai, V.; Sichelschmidt, J.; Zakharov, D.; Kaul, E.; Geibel, C. ESR study of the anisotropic exchange in the quasi-one-dimensional antiferromagnet Sr 2 V 3 O 9. *Phys. Rev. B* **2003**, *68*, No. 064404.

(58) Li, X.; Zhang, H.; Mai, Z.; Zhang, H.; Vankelecom, I. Ion exchange membranes for vanadium redox flow battery (VRB) applications. *Energy Environ. Sci.* **2011**, *4*, 1147−1160.

(59) Zhiyu, Q.; Pierre, T. Electrochemical reduction of niobium ions in molten LiF-NaF. *J. Appl. Electrochem.* **1985**, *15*, 259−265.

(60) Fiore, M.; Orecchio, S.; Romano, V.; Zingales, R. Redox potentials of vanadium-containing couples. Part 3. The formal redox potential of the V3+−V2+ couple. *J. Chem. Soc., Dalton Trans.* **1993**, *5*, 799−802.